



# The Temperature Dependence of Hot Prograde Flows in Solar Active Regions

Jimmy C. Fitzpatrick<sup>1</sup> · Hugh S. Hudson<sup>1,2</sup>

Received: 3 October 2022 / Accepted: 7 December 2022  
© The Author(s) 2022

## Abstract

Using simultaneous observations from the *EUV Variability Experiment* (EVE) and imaging from the *Atmospheric Imaging Assembly* (AIA), we characterise the temperature dependence of apparent hot flows in solar active regions. The EVE instrument performs Sun-as-a-star spectroscopy and is composed of two spectrographs: MEGS-A and MEGS-B (*Multiple EUV Grating Spectrograph-A, -B*). It is known that EVE can measure wavelength shifts and thus can observe relative Doppler velocities in solar atmospheric plasmas over an extended temperature range. However, MEGS-A is affected by a known astigmatism effect (Chamberlin: *Solar Phys.* **291**, 1665, 2016); inhomogeneities in EUV brightness on the solar surface result in purely instrumental wavelength errors. We validate our methods by independently quantifying this effect and comparing to Chamberlin's results, and we explore the wavelength dependence as an extension of his formula as derived for He II 304 Å. MEGS-B is unaffected by this instrumental effect in any case, and this has allowed us to find evidence of hot prograde flows in active regions. Using our image-based models for the astigmatism and flows, we independently confirm our original MEGS-B result. We now extend our knowledge of the temperature dependence of these flows via the additional Fe emission lines available in MEGS-A. We find a monotonic increase of apparent flow speed with temperature up through lines of Fe XVI, nominally formed at about 6.4 MK.

**Keywords** Sun: corona · Sun: UV radiation · Sun: activity

## 1. Introduction

In recent years, spectroscopy in extreme ultraviolet (EUV) wavelengths has developed many applications for measuring plasma motions in the solar atmosphere. The *EUV Variability Experiment* (EVE: Woods et al., 2012) residing onboard the *Solar Dynamics Observatory* (SDO: Pesnell, Thompson, and Chamberlin, 2012) has been providing spectra since 2010

---

✉ H.S. Hudson  
[hugh.hudson@glasgow.ac.uk](mailto:hugh.hudson@glasgow.ac.uk)

J.C. Fitzpatrick  
[jcfitzpatrick12@gmail.com](mailto:jcfitzpatrick12@gmail.com)

<sup>1</sup> SUPA School of Physics and Astronomy, University of Glasgow, Glasgow G12 8QQ, UK

<sup>2</sup> SSL, University of California, Berkeley, CA, USA

in the range (5 – 105 nm) with good spectral resolution (0.1 nm) and high temporal cadence (10 seconds). Its stability and precision allow for sensitive wavelength shifts to be detected, thus providing a solid framework for many solar-physics studies in EUV spectroscopy for the “Sun as a star,” i.e. without image information.

One of the first significant solar-physics contributions from the EVE spectroscopy demonstrated that one can derive relative Doppler velocities of flaring plasma using EVE spectra (Hudson et al., 2011). The stability of the measurements is visibly demonstrated in the detection of the orbital motion of SDO, through measured wavelength shifts of the bright He II 304 Å emission line. This was possible despite the coarse spectral bin-width (0.4 Å, some  $400 \text{ km s}^{-1}$  in Doppler speed), much larger than the magnitude of the orbital shifts. Brown, Fletcher, and Labrosse (2016) used EVE spectral measurements to measure relative wavelength shifts of MEGS-B lines during solar flares. This study provided evidence for both upflows and downflows of the higher Lyman-series lines ( $\beta$ ,  $\gamma$ ,  $\delta$ ) as Doppler shifts. Related analysis by Cheng et al. (2019) also used multiple EVE-observed emission lines to investigate the temperature dependence of Doppler shifts during two X-class flares near the solar disk center.

As well as short-term observations of transient solar events, the continuous coverage from EVE enables analysis of long-term variations of the global Sun. Solar EUV spectral irradiance varies from time scales of seconds to minutes (flaring timescales), to days and weeks (emergence and rotation of active regions), to years and greater from global changes during the solar cycle. Recent analysis over these longer time scales (Hudson et al., 2022) yielded a surprising property of hot plasmas in solar active regions. Long time-series of wavelength shifts of EUV emission lines, in conjunction with AIA (*Atmospheric Imaging Assembly*) imagery, also onboard SDO, revealed apparently ubiquitous hot prograde flows. This article extends these results. Cheng, Wang, and Liu (2021) had also performed a time-series analysis of multiple lines over a four-month period investigating instrumental effects, as discussed below. These instrumental effects alter the wavelength shifts of emission lines over a subset of the wavelength range covered by EVE, and they are another principal focus of this article.

The EVE/MEGS instrument (*Multiple EUV Grating Spectrometer*) consists of three different channels: MEGS-A1, MEGS-A2 ( $\approx 65\text{--}370 \text{ \AA}$ ), and MEGS-B ( $\approx 370\text{--}1060 \text{ \AA}$ ) obtaining a solar spectrum every ten seconds with a nearly 100% duty cycle (Woods et al., 2012; Pesnell, Thompson, and Chamberlin, 2012). The MEGS-A and -B instruments operated from 2010 to 2014; MEGS-B continues to operate but with a reduced duty cycle and with time bins increased to 60 seconds. MEGS-A is a compact grazing-incidence spectrograph with some astigmatism as designed (Crotser et al., 2007). The combination of the full-disk spectra and off-axis contributions thus results in small distortions of the wavelength calibration. Operationally, this calibration depends upon the observed spectra and information from the spectral atlas CHIANTI (Dere et al., 1997). EVE meets all off-axis imaging requirements necessary for its principal science aim of spectral-irradiance characterization, and this off-axis sensitivity is well documented by Crotser et al. (2007). Notably, astigmatism in the optics does not affect lines observed by MEGS-B, but strongly does so in MEGS-A, where this effect causes instrumental wavelength shifts that compete with the Doppler information.

Hudson et al. (2011) noted this effect and presented an approximate equation to correct for the offset given the location of a flare event on the solar disk. Chamberlin (2016) definitively characterized the astigmatism by performing a detailed analysis of the necessary corrections for the He II 304 Å line, calibrated in orbit by using the quarterly “cruciform scans” carried out via SDO pointing offsets. However, this derivation provides only the correction assuming uniform solar images and does not account for global inhomogeneities in

EUV brightness over the solar disk. This is a vital consideration since each component of the solar disk contributes a different wavelength offset to any (disk-integrated) spectral line observed by MEGS-A. However, EVE has no spatial resolution, and thus we must turn to other sources of image data to quantify this instrumental effect more completely.

In this article, we build on the work of Chamberlin (2016) and similar work by Cheng, Wang, and Liu (2021) by using AIA images to develop a method to quantify this instrumental astigmatism and compare to the previous estimates. We extend the work of Hudson et al. (2022) by modelling the hot flows using emission lines observed by MEGS-A and MEGS-B over a broad range of wavelengths and temperatures. This analysis makes it possible to use many additional EVE/MEGS-A spectral lines for Doppler measurements. The analysis here relies entirely on the calibrated EVE data products, rather than the raw data.

## 2. Characterisation of MEGS-A Astigmatism via Image Centroids

### 2.1. The Nature of the Problem

As discussed above, wavelength shifts of lines observed using MEGS-A are affected by astigmatism in the optics. Inhomogeneities in EUV brightness on the solar surface can thus lead to purely instrumental wavelength shifts, not attributed to any physical plasma motions. As demonstrated by Cheng, Wang, and Liu (2021) for example, this gives the appearance of oscillatory structures in longer time series of line centroids. In this case, the wavelength shifts exhibit a positive correlation with expected variations from astigmatism due to the rotation of active regions across the solar surface. Surprisingly, as shown graphically by Hudson et al. (2022), similar oscillatory structures are present in the wavelength shifts of hot lines observed by MEGS-B, where the effects of the astigmatism are negligible (Woods et al., 2012). Hudson et al. (2022) provide strong evidence to suggest that these temporal structures result from hot prograde flows confined to active regions. The combination of these two effects leads to a difficult modelling problem for MEGS-A, where many spectral lines reflect higher temperatures than those in the MEGS-B band. It is clear that the structure of a line-centroid time series observed with EVE is intrinsically linked with activity in active regions, with both the astigmatism and flow-like components contributing to the variability. Any Doppler interpretation of a hot line observed with MEGS-A is thus affected by both the astigmatism and flows simultaneously.

In order to disentangle the two effects, a generalised mathematical framework is required. Chamberlin (2016) gives a correction formula for this astigmatism, valid for the He II 304 Å line:

$$\Delta\lambda_{\text{corr}} = \alpha(t) \sin^2(E - W) + \beta(t) \sin(N - S). \quad (1)$$

This formula provides the wavelength correction  $\Delta\lambda$  for Doppler measurements of an isolated, bright and localised source located at heliographic longitude and latitude coordinates. The quadratic term reflects the fact that the spectrographic dispersion is almost exactly in the image EW direction. Note that Equation 1 assumes south and west coordinates as positive and north or east as negative. Gradual CCD degradation resulted in some temporal dependence, represented here by  $\alpha(t)$  and  $\beta(t)$ . The corrected wavelength is then found from  $\lambda = \lambda_{\text{obs}} - \Delta\lambda_{\text{corr}}$ . Note that first term refers to the dispersion direction of the EVE gratings, the second to the cross-dispersion direction, and that the adopted functional dependencies follow those of Chamberlin (2016). Equation 1 contains no brightness information and is to be applied under the assumption that the source dominates the line emission at that time. In

other words, we assume that the observed line emission comes from an off-axis point source located at unique coordinates, and that the global inhomogeneities in EUV brightness (such as active regions) therefore offer negligible contributions to the wavelength shift. It is clear now that this assumption must be invalid, strictly speaking, and that the interpretation of the data from the cruciform scans generally depends on the offpointing amplitude and solar image details.

SDO's *Atmospheric Imaging Assembly* (AIA) provides many simultaneous full-disk images of the corona and transition region up to heights of  $0.5 R_{\odot}$  above the solar limb, and performs at a high spatial ( $1.5''$ ) and temporal (12 seconds) resolution (Lemen et al., 2012). In order to account for image brightness inhomogeneities, we can use AIA imaging to approximate the monochromatic intensity distributions of different lines in MEGS-A and MEGS-B. The images thus let us sum over the wavelength-shift contributions from each pixel, with each contribution weighted by the pixel intensity. Thus, a more general correction formula is well described by

$$\Delta\lambda_{\text{AIA}} = \frac{1}{I_{\text{tot}}} \sum_{i,j} I_{ij} f(\tilde{x}_{ij}, \tilde{y}_{ij}, t), \quad (2)$$

where  $f(\tilde{x}_{ij}, \tilde{y}_{ij}, t)$  is the correction function accounting for wavelength-shift contributions from the  $[i, j]$ th pixel being off-axis at location  $\tilde{x}_{ij}, \tilde{y}_{ij}$  (arbitrary coordinates), and  $I_{ij}$  being the intensity at the  $[i, j]$ th pixel. The sum is performed over all the pixels and normalised to the integrated intensity  $I_{\text{tot}} = \sum_{i,j} I_{ij}$ . This equation measures the *overall* correction to wavelength shift caused by contributions from the whole solar disk. A verification can be made that this formula reduces to Equation 1 with  $f(\tilde{x}_{ij}, \tilde{y}_{ij}, t) = \alpha(t) \sin^2(\tilde{x}_{ij}) + \beta(t) \sin(\tilde{y}_{ij})$  with  $\tilde{x}_{ij} = (E - W)_{ij}$ ,  $\tilde{y}_{ij} = (N - S)_{ij}$  being the heliographic coordinates of the  $i, j$ th pixel; and an intensity distribution describing a single pixel of intensity  $I$  at pixel  $[p, q]$  such that  $I_{ij} = I \delta_{ip} \delta_{jq}$  using the Kronecker delta.

Naturally, Equation 1 is restricted to on-disk events due to the use of heliographic coordinates, and this convention has been continued in subsequent literature by Cheng, Wang, and Liu (2021). Chamberlin (2016) notes that the equation can be extended to above-limb events by converting it to helioprojective coordinates (the SDO offpointing angles). This is a significant point; when using heliographic coordinates in Equation 2, contributions from above-limb pixels are necessarily excluded, since the locations of these pixels are undefined in this coordinate system. We show an example of this effect in Figure 1.

Contributions of the astigmatism and also the prograde flow component are largest for activity at or above the limb. This can be seen in the figures in Hudson et al. (2022): in the purely astigmatic case, Equation 1 shows that maxima correspond symmetrically to activity at either limb; the prograde flows instead have an asymmetric character: positive at the E and negative at the W. Furthermore, any emission from coronal loops extending above the solar surface at the limbs would be misrepresented by the use of heliographic coordinates. It is exactly in these regions of strong contributions where the pixel-clipping occurs. For this reason, in the following analysis we use standard helioprojective coordinates. This system uses heliographic angles measured from the apparent disk centre, as seen by an observer, and we use the sign convention defined earlier. For a review of the relevant coordinate systems discussed, see Thompson (2006).

For our analysis, we present the generalised correction formula for  $f$  in Equation 2 according to

$$f(X_{ij}, Y_{ij}) = \underbrace{C_0 Y_{ij} + C_1 X_{ij}^2}_{\text{Astigmatism}} + \underbrace{C_2 F(X_{ij})}_{\text{Flow}} + C_3 t, \quad (3)$$

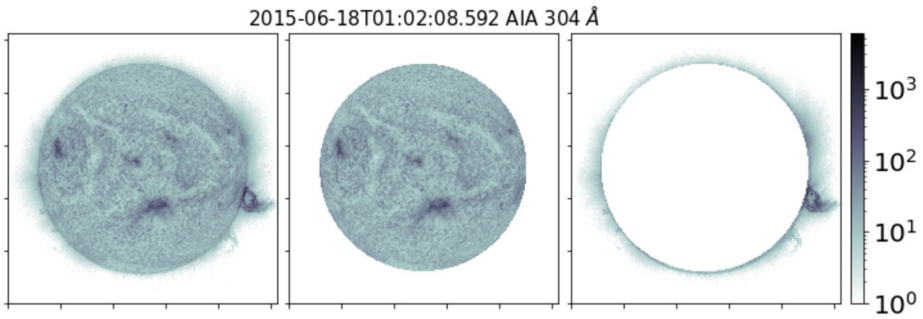


**Figure 1** An example of pixel clipping for an AIA image at 304 Å, 18 June 2015 01:02:08.592 UT. The *left panel* shows the raw image data (log display to show faint features). The *middle panel* shows the pixels that contribute to the correction using heliographic coordinates; the *right panel* shows the pixels discarded. In particular, note the large coronal loop at the west limb, of comparable brightness to the disk features; the feature would make no contribution to the overall correction using heliographic coordinates. Using helioprojective coordinates we can make use of the full image.

where  $C_i$ ,  $i \in \{0, 1, 2, 3\}$  are constant coefficients;  $X_{ij}, Y_{ij}$  are the helioprojective coordinates of the  $[i, j]$ th pixel, normalised to the solar radius

$$X_{ij} = \frac{X_{ij}}{R_{\odot}}, \quad Y_{ij} = \frac{Y_{ij}}{R_{\odot}}, \tag{4}$$

and  $t$  is the fraction of a year since 2010.4, when SDO began normal operations. Equation 3 describes the wavelength-shift contribution of a single pixel at the coordinates  $X_{ij}, Y_{ij}$ . It is thus flexible enough to allow for above-limb contributions, to account for both astigmatism ( $C_0$  and  $C_1$ ) and a simple flow term  $C_2$  to the wavelength shifts, and to allow for a time-dependent background term  $C_3$ . The latter can account for slow variations not quantified by the flow and astigmatic terms and possibly related to instrument degradation (Chamberlin, 2016).

When fitting this model to data, naturally the size of these coefficients is contingent on the choice of units. All fitted variables listed in Tables 3, 4, and 5 reference models describe picometre wavelength shifts, to remain consistent with Chamberlin (2016). Accordingly, in the relevant figures in Section 2.3 onwards, we make implicit conversions to Å and multiply the model shifts by a factor of 0.01.

The flow function  $F(X_{ij})$  is the simplest possible model; we will discuss this further in Section 3. Generally we confirm the previous estimates of the astigmatism correction of Chamberlin (2016), and we find evidence of flow-like components by parameter fitting appropriate coefficients  $C_i$  in Equation 3 to the wavelength shifts of many lines observed by EVE. This will be described in detail in the following sections.

## 2.2. A Fitting Method for Time-Series Data

Standard approaches to fitting the spectroscopic data must be extended to allow for the complexity of the competing time-domain effects (astigmatism, high-speed flows, image degradation). In the present context, we have no specific interest in the details of the line formation, but rather in the global dynamics as measured by the line centre. We thus employ the simpler “centre-of-mass” approach to extract the intensity-weighted centroid, according

to

$$\bar{\lambda}(t) = \sum_i \frac{\lambda_i I(\lambda_i, t)}{\sum_i I(\lambda_i, t)}. \tag{5}$$

Here for a given time  $[t]$ , we have that  $\bar{\lambda}(t)$  is the computed centroid of the line; the actual observable is the line displacement  $[\bar{\lambda}(t) - \bar{\lambda}_0]$ , with the choice of  $\bar{\lambda}_0$  to be discussed below.  $I(\lambda_i, t)$  is the intensity measured at the  $i$ th spectral bin. The range of wavelengths over which this method is evaluated are the EVE spectral bins located nearest  $[\lambda_0 - \lambda_{\text{tol}}, \lambda_0 + \lambda_{\text{tol}}]$ , where  $\lambda_{\text{tol}}$  is an adopted spectral range around  $\lambda_0$ , chosen to optimize the isolation of the given line. This value is chosen such that it is sufficient to cover the wings of the line profile, but minimise contributions of other lines. This method has been used by Brown, Fletcher, and Labrosse (2016), noting that inferred Doppler velocities from this method only determine actual line-of-sight speeds relative to the wavelength calibration. We thus obtain a time-series of wavelength shifts that will allow us to parameter-fit the coefficients  $C_i$  for a model such as that described in Equation 3.

In the following, we generally adopt an arbitrary choice for  $\lambda_0$  and  $\bar{\lambda}_0$ . The former is used as an initial estimate of the line centre and is used to define the bounds over which the centre-of-mass approach is evaluated. The latter represents the median of the observed line position  $[\bar{\lambda}(t)]$ , for a given time interval; or simply the database wavelength as interpreted on the default wavelength scale of the observations. We cannot refer to a precisely known apparent wavelength for any of the lines, because the precision of the measurements exceeds the absolute accuracy of the wavelength calibration. Indeed, the in-flight calibration of the wavelength scale depends on some of the very lines that show the complicated time-domain shifts that we study here.

To carry out the parameter fitting of the coefficients  $C_i$ , we perform a brute-force grid-search in parameter space for the best fit. On a pixel-by-pixel basis, this would be computationally infeasible for the time-series of AIA images that we use in this study. Through simple algebraic manipulation, Equation 2 can be transformed into the equivalent

$$\begin{aligned} \Delta\lambda_{\text{AIA}} &= C_0 \sum_{i,j} \frac{I_{ij} Y_{ij}}{I_{\text{tot}}} + C_1 \sum_{i,j} \frac{I_{ij} X_{ij}^2}{I_{\text{tot}}} + C_2 \sum_{i,j} \frac{I_{ij} F(X_{ij})}{I_{\text{tot}}} + C_3 t \\ &= C_0 \bar{Y}^1 + C_1 \bar{X}^2 + C_2 \bar{F} + C_3 t, \end{aligned} \tag{6}$$

with the time-dependent term unchanged, since  $\sum_{i,j} I_{ij} / I_{\text{tot}} = 1$ . In writing Equation 6, we show that the pixel-by-pixel summation of wavelength contributions is equivalently characterised by the general image centroids defined by the sums. In another sense, we are assuming that the time series of wavelength shifts is well decomposed into the basis functions  $\bar{X}^2(t)$  and so on. This approach provides the advantage that the coefficients are computed for each AIA image prior to the parameter searches. This form of the correction formula can ignore any tilt-angle correction of the Earth relative to the Sun (the  $B_0$ -angle). Note that the single parameter of the flow term grossly simplifies the physical picture.

In order to find the best fits in the grid-search, we employ an inspection-of-residuals method akin to that suggested by Andrae, Schulze-Hartung, and Melchior (2010). We prefer this fitting procedure to other commonplace methods such as the reduced  $\chi^2$ -procedures, and minimisation of the mean-square error as used by Cheng, Wang, and Liu (2021). Andrae, Schulze-Hartung, and Melchior reason that the reduced  $\chi^2$ -method should not be used for non-linear models, such as the SDO ephemeris term as described below in Equation 7.

Indeed, the method should likewise not be employed if the basis functions of the model are not linearly independent. For example, there is no guarantee that the simplified flow-term  $\overline{F}(t)$ , as defined in Equation 6 and later Equation 12, should be linearly independent of the quadratic astigmatism term  $\overline{X}^2(t)$  in the positive hemispheres.

The procedure for the inspection-of-residuals parameter modelling is simply defined. For each combination of coefficients  $C_i$  in the grid-search, we have the corresponding wavelength-correction  $[M(t_n)]$  computed from the  $n$ th AIA image in the series captured at time  $t_n$ . Consider  $r_n = M(t_n) - \overline{\lambda}(t_n)$  to be the  $n$ th residual of the model with the simultaneously measured EVE centroid of the specified emission line. If we have  $N$  data points, for this model we will have a distribution of  $N$  residuals,  $R = \{r_0, r_1, \dots, r_N\}$ . As we find the uncertainties in the measured EVE wavelength shifts to be approximately Gaussian, one would expect for a good fit that the distribution of residuals  $R$  would also be approximately Gaussian with a similar variance. The “best-fit” model is one that maximises the similarity between  $R$  and a specified Gaussian distribution; we will describe the form of the latter below. This measure of similarity is quantified for each model by performing the two-sample Kolmogorov–Smirnov (hereafter KS) test between  $R$  and a normally distributed pool of  $N$  random variables (Kolmogorov, 1933; Smirnov, 1948; Hodges, 1958), and we compute the p-value statistic for each model in the grid-search.

The KS test compares cumulative distribution functions in a model-independent manner, and its probability estimation (“p-value” here) is a standard goodness-of-fit variable. Finding the global maximum of the KS p-value in parameter space will yield the residual distribution most closely resembling the specified Gaussian, and thus provide the best-fit parameters  $[C_i]$  by this definition. In the case where a number of parameters equally maximise the statistic, we take the median as the output.

For numerical stability, we normalise the model and the measured data so that a specific characterisation of the measured error  $\varepsilon$  is equal to unity. For each model, we then compute the KS p-value between  $R$  and a normally distributed pool of mean 0 and variance 1. In practice, the residual distributions are multiplied by a factor of  $1/\varepsilon$ . This procedure is equivalent to retaining the original units and comparing  $R$  to a normally distributed pool of mean zero and variance  $\varepsilon$ . The value  $\varepsilon$  can be regarded as an estimate of the expected variance between an ideal model and the measured data. In most cases, it suffices to take  $\varepsilon$  as the minimum or the median of the measured errors of the data to be modelled. Specifically, for an uncertainty distribution of the EVE wavelength shifts, say  $U$ , over a particular time range, the output-parameters of the fitting procedure are found to be stable to perturbations and provide the best fits in the range  $[\min(U) < \varepsilon < \text{median}(U)]$ . Figure 2 demonstrates this, showing the dependence of output parameters during astigmatism fitting of He II at 303.8 Å and 256.3 Å using different values of  $\varepsilon$  in this neighbourhood. We describe these fittings in detail in Section 2.3. These results are as expected. For example, taking  $\varepsilon$  too small or too large with respect to this range can lead to numerical instabilities in the KS test.

We quantify the uncertainties and improve the robustness of the fitting using empirical methods. The developed “bootstrapping” procedure (e.g. Andrae, 2010; Andrae, Schulze-Hartung, and Melchior, 2010) involves taking random samplings of the residual distribution, allowing for repeats, and performing the maximisation of the KS statistic for each resample. For each bootstrap resample  $b$ , we compute the output parameters  $\{C_i\}_b$ ,  $i \in \{0, 1, 2, 3\}$  that maximise the KS p-value statistic in each case. The *final* output parameters are defined as the median of the bootstrap distribution for each output parameter. The uncertainty is listed as the maximum between the standard deviation of the same distribution, and the grid-spacing for the respective parameters. Although there are more powerful statistical tests of normality (e.g. Mohd Razali and Yap, 2011), we find the KS p-value statistic to suffice in this case.

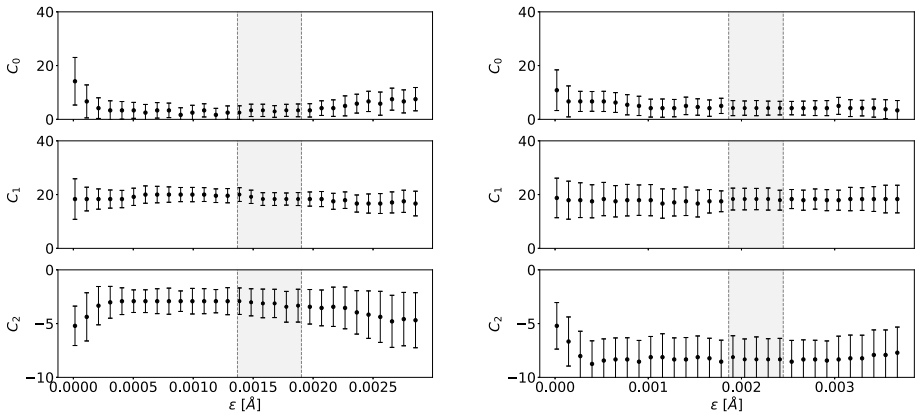


**Figure 2** The dependence of the output parameters on the value of  $\epsilon$  during astigmatism fittings to He II at 303.8 Å (left panels) and 256.3 Å (right panels) wavelength shifts. The fittings are identical to those described in Section 2.3. In each panel, the grey-shaded region denotes the range  $\min(U) < \epsilon < \text{median}(U)$ , where  $U$  is the measured uncertainty distribution of the EVE wavelength shifts in each case. We observe that outside the suggested ranges, deviations in output parameters may be expected. Error-bar construction and fitting procedure are described in Section 2.2.

We demonstrate the utility of this method in extracting the orbital characteristics of SDO through wavelength shifts of the Lyman- $\gamma$  line at 972.5370 Å observed using MEGS-B. MEGS-B is free of astigmatism, and from our experience such a low-temperature line should have a minimal flow term. For details of the parameters used to extract the centroids, see Table 1.

We assume a line-of-sight velocity model of the form

$$\Delta v \text{ [km s}^{-1}\text{]} = C_0 t + C_1 \sin\left(\frac{2\pi t}{C_2} + C_3\right), \tag{7}$$

where  $t$  is in days,  $C_0$  is the slope of the linear background term;  $C_1$ ,  $C_2$ ,  $C_3$  denote the amplitude [km s<sup>-1</sup>], period [days], and phase [rad] respectively. We perform a grid-search over the parameter ranges  $C_0 \in [-1, 1]$ ,  $C_1 \in [1, 10]$ ,  $C_2 \in [0.6, 2.5]$ ,  $C_3 \in [0, \pi]$ , and consider 15 equidistant samples in these ranges. Note that the four  $C_i$  parameters now fit different functional terms from their original use in Equation 3. The best fit is evaluated using the inspection-of-residuals method as described above, with the procedure iterated over 100 bootstrap resamples of the residuals. We find that for the periodic term  $C_2$ , it is necessary that the grid-search include a period close to that of the source (for these data, the expected value is naturally  $C_2 = 1$ ).

This is not an issue for the astigmatism and flow modelling in the following sections, where the periods are well encoded in the image-centroid basis functions and no period fitting is required. Further, in this case the median of the measured uncertainties of the wavelength shifts are of the same size of the amplitude of the oscillation (both around  $\approx 3 \text{ km s}^{-1}$ ). Values of  $\epsilon$  satisfying  $[\min(U) < \epsilon < 3 \text{ km s}^{-1}]$  are sufficient to characterise the wavelength shifts with this model.

Figure 3 shows the fit results (Table 2). The inspection-of-residuals procedure successfully extracts the expected orbital motion of SDO, and matches well with the expected shifts from the JPL Horizons tool ([ssd.jpl.nasa.gov/horizons](http://ssd.jpl.nasa.gov/horizons)). Figure 4 presents slices of the KS p-value surface in parameter space for two different bootstrap resamples of the residuals.



**Table 1** The line parameters used for centroid extractions throughout the study. *Left to right the columns indicate: name of the ion; line centre as listed in the CHIANTI database (Dere et al., 1997);  $\log(T_{\max})$  as listed in the CHIANTI database,  $\lambda_0$ ,  $\lambda_{\text{tol}}$  are as in Section 2.3; indicated data-points have been averaged  $\Delta t_{\text{av}}$  seconds prior to the data-point; the MEGS instrument which observes the given line.*

Ion	$\lambda_{\text{CHIANTI}} [\text{\AA}]$	$\log(T_{\max})$	$\lambda_0 [\text{\AA}]$	$\lambda_{\text{tol}} [\text{\AA}]$	$\Delta t_{\text{av}} [\text{s}]$	MEGS
Fe IX	171.0730	5.9	171.05	1.0	720	MEGS-A
Fe XI	182.1670	6.2	182.20	0.7	720	MEGS-A
Fe XII	195.1190	6.2	195.10	0.8	720	MEGS-A
Fe XIII	209.6190	6.3	209.81	0.7	720	MEGS-A
Fe XIV	211.3170	6.3	211.45	0.8	720	MEGS-A
He II	256.3170	4.9	256.20	0.7	720	MEGS-A
Fe XIV	274.2030	6.3	274.175	0.7	720	MEGS-A
Fe XV	284.1630	6.8	284.10	1.0	720	MEGS-A
He II	303.7800	4.9	303.80	2.0	720	MEGS-A
Fe XVI	335.4090	6.8	335.40	0.9	720	MEGS-B
Fe XVI	360.7500	6.8	360.9	0.8	720	MEGS-B
Mg IX	368.0710	6.0	368.10	1.2	720	MEGS-B
Si XII	499.4060	6.9	499.50	1.2	720	MEGS-B
Si XII	520.6650	6.9	520.66	0.8	720	MEGS-B
Mg X	609.7930	6.8	609.90	1.0	720	MEGS-B
Mg X	624.9410	6.8	625.00	1.2	720	MEGS-B
Ne VIII	780.3850	5.8	770.50	1.2	720	MEGS-B
Lyman- $\gamma$	972.5370	4.5	972.60	2.0	2880	MEGS-B

**Table 2** The output parameters from Equation 7, giving the results shown in Figure 3, and the magnitude of  $\varepsilon$  used in this particular parameter search.

$C_0$	$-0.14 \pm 0.14$	$\text{km s}^{-1} \text{ day}^{-1}$
$C_1$	$3.57 \pm 0.65$	$\text{km s}^{-1}$
$C_2$	$1.01 \pm 0.14$	days
$C_3$	$1.80 \pm 0.22$	rad
$\varepsilon$	1.042	$\text{km s}^{-1}$

Slices are taken near the global maximum for each resample. A sharp increase in p-values as the periodicity parameter  $C_2$  approaches unity is easily distinguished in each case, and the exact slices containing the global maxima for each residual resample are indicated in the red-outlined plots.

### 2.3. Fits for the MEGS-A Astigmatism

Using the methods described above, we now quantify the MEGS-A astigmatism and compare it with the previous estimates by Chamberlin (2016). We focus initially on the He II line emissions at 303.8  $\text{\AA}$  and 256.3  $\text{\AA}$ . For these lines, we use AIA images from the 304  $\text{\AA}$  passband as a first approximation for the true monochromatic EUV intensity distributions. The He II line at 303.8  $\text{\AA}$  is by design the primary contributor of the 304  $\text{\AA}$  AIA passband (Lemen et al., 2012). Indeed, O'Dwyer et al. (2010) finds that for AR and QS plasma, the 303.8  $\text{\AA}$  line definitely dominates this channel. For sources above the limb, projected against the corona, we expect this AIA channel to have a significant contribution from the higher-

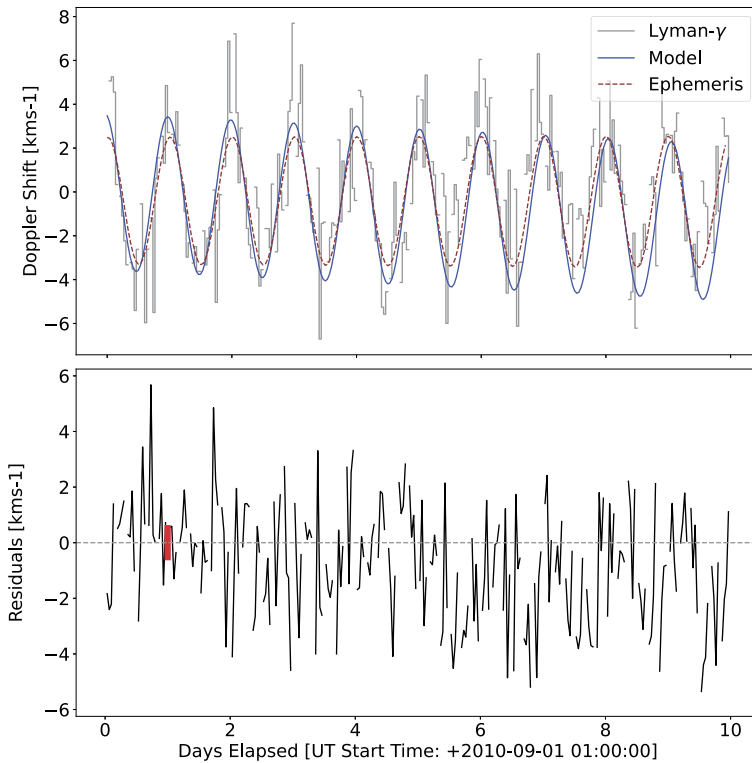


**Figure 3** The output of the example fitting for the SDO orbital motion, using Lyman- $\gamma$  at  $972.54 \text{ \AA}$ . The *top panel* presents the output of the inspection-of-residuals fitting (*blue*), overlaid on time-averaged Lyman- $\gamma$  centroids (*grey*) and the expected orbital shift from the ephemeris data (*dashed brown*). For details of the extraction of the line centroids, see Table 1. The *bottom panel* displays the residuals (*black*) taken between the output model and the Lyman line shifts. The *red bar* in the bottom panel denotes the equivalent variance of the comparative Gaussian [ $\varepsilon$ ] as described in the text. The respective parameters of the output model are listed in Table 2.

temperature Si II line at  $303.33 \text{ \AA}$ , and with a small flare-like responses due to Ca XVIII at  $302.19 \text{ \AA}$ , these effects should be minimal; we conclude that the AIA  $304 \text{ \AA}$  is a good proxy for an (unavailable) time series of monochromatic images.

The raw wavelength shifts of these lines exhibit variations on many time scales, well-demonstrated in Figure 5. For these data, slow year-scale secular variations are visible, as well as the approximately two-week periodic oscillations attributed to AR rotation and the MEGS-A astigmatism. We suggest that the former slower variations could result from slow shifts of the signal's diurnal artifact. However, determining the exact nature of this essentially magnetospheric effect is beyond the scope of this study. We adopt a simple treatment of the slow-varying component by including a linear background term in the model fittings.

We consider first the subset of the 2013 epoch bounded by the vertical grey dashed lines in Figure 5, from 1 May 2013 to 12 July 2013 UT. For these studies we use data from 17:00–18:00 UT; this hour puts the SDO spacecraft close to the Earth–Sun line, and hence minimizes its orbital Doppler effect. Our minimal model describes both the astigmatism and

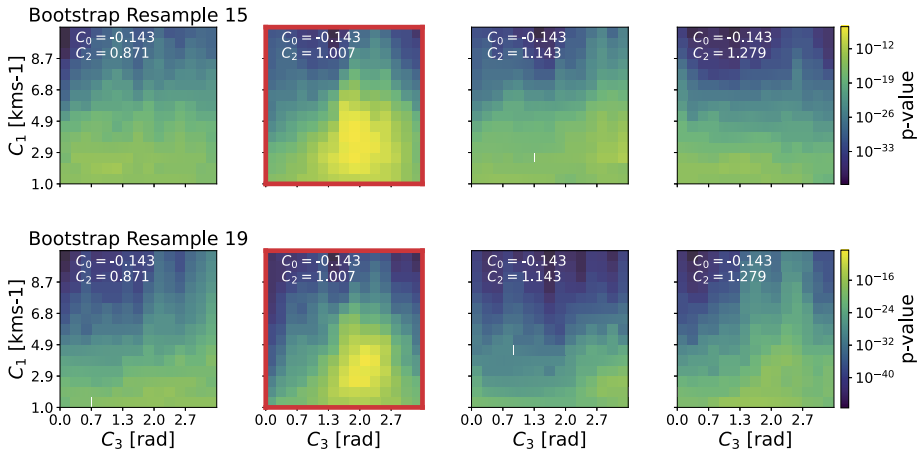


**Figure 4** Cross-sections of the p-value surface in parameter space near the global maxima for specific bootstrap resamplings of the residuals. Each pixel denotes a model with respective coefficients  $[C_i]$  depending on its coordinates in this space. Log-normalised intensities denote the magnitude of the KS p-value for each model. The *top row* and *bottom row* denote slices of the surface for two different bootstrap resamplings of the residual distribution. All surfaces plotted are held at constant  $C_0 = -0.143$ , and *increasing column number corresponds to increasing period:  $C_2$* . The *red outlined subplots* contain the global maxima for each surface and show the sharp increase in p-value observed for  $C_2 \approx 1$ , the (normalised) orbital period of SDO.

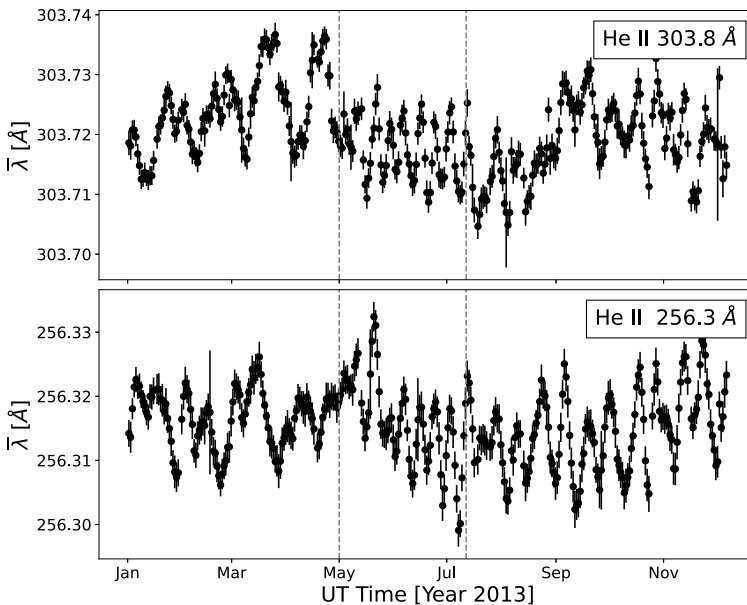


**Figure 5** The wavelengths shifts of the He II lines at 303.8 Å (*top panel*) and 256.3 Å (*bottom panel*) over the year 2013. Clear year-scale variations are visible, along with the variations attributed to the MEGS-A astigmatism. The equivalent Doppler root mean square (RMS) is approximately 6–7 km s<sup>-1</sup> for each of the line-motions shown. “Centre-of-mass” extraction parameters are listed in Table 1. For both lines, centroids are sampled between 17:00 and 18:00 UT daily. *Grey dashed lines* denote the subset modelled in Figures 6 and 7.

**Table 3** Output parameters from Equation 8 for the astigmatism fittings presented in Figures 6 and 7, and the value  $\varepsilon$  used in the parameter searches.

	He II 303.8 Å	He II 256.3 Å	
$C_0$	$4.17 \pm 3.30$	$5.00 \pm 2.71$	pm
$C_1$	$17.50 \pm 2.68$	$18.33 \pm 3.34$	pm
$C_2$	$-3.75 \pm 1.90$	$-8.59 \pm 1.90$	pm yr <sup>-1</sup>
$\varepsilon$	0.0019	0.0024	Å

the slow-varying background:

$$\Delta v_{\text{AIA}} [\text{pm}] = C_0 \bar{Y}^1(t) + C_1 \bar{X}^2(t) + C_2 t, \quad (8)$$

where the variables are the same as in Equation 6, but again with different  $C_i$  assignments. The Chamberlin (2016) description of the astigmatism, confirmed by our independent investigation, contains the linear term in  $Y$  and quadratic term in  $X$  and no others. The secular term is as described above, and  $t$  is in Chamberlin's time units: the fraction of year since 2010.4, the approximate time SDO began operations. The flow term has been omitted. This reflects our conclusion that mainly higher-temperature plasmas reveal the flow phenomenon. In an analogous procedure to the orbital fitting, we perform a parameter search over the ranges  $C_0, C_1 \in [0, 40]$  and  $C_2 \in [-10, 0]$ . In this we make no assumptions on the relative magnitudes of  $C_0$  and  $C_1$ . A negative slope for the secular term is assumed. We consider 25 equidistant samples in the above ranges, and iterate the bootstrapping procedure over 100 resamplings of the residual distributions. The parameter modelling was performed identically for the line centroids sampled for both 303.8 Å and 256.3 Å.

The results are presented in Figures 6 and 7, and it is clear that the oscillatory component of the wavelength signal for both lines is well described by our model of the instrumental astigmatism. From this point onward, the "Chamberlin model" is defined as

$$\bar{A}(t) = \begin{cases} (4.14 + 0.0064t)\bar{Y}^1(t) + (16.37 + 5.56t)\bar{X}^2(t) & t < 12 \text{ March 2012,} \\ (4.21 + 0.0060t)\bar{Y}^1(t) + (14.40 + 3.49t)\bar{X}^2(t) & t > 12 \text{ March 2012,} \end{cases} \quad (9)$$

where  $t$  is identically in Chamberlin's time units and  $\bar{A}(t)$  is in picometres. The discontinuity time, as well as the astigmatism coefficients, are those that he derived from data obtained during the SDO cruciform scans; this will be expanded on in the section following. For both lines, it appears that the Chamberlin model slightly overestimates the amplitude of the variations. This fact is also present in the consistent slight decrease in the fitted quadratic coefficients in Figure 9. Cheng, Wang, and Liu (2021) also find a slight decrease in the quadratic coefficient using similar methods. These discrepancies will be discussed further in the following section. We discuss a possible wavelength dependence of the astigmatism correction in Section 3.2.

## 2.4. Image-Based Confirmation of the Cruciform Scan Results

By performing a similar analysis, we characterise the temporal dependence of the astigmatism coefficients for He II 303.7860 Å and compare to previous estimates. Chamberlin (2016) quantifies the astigmatism by using the quarterly cruciform scans performed by SDO. These on-orbit calibrations involve offsetting the pointing of SDO at regular intervals and an estimate of the astigmatism is obtained by measuring the centroids of the distorted line profiles.

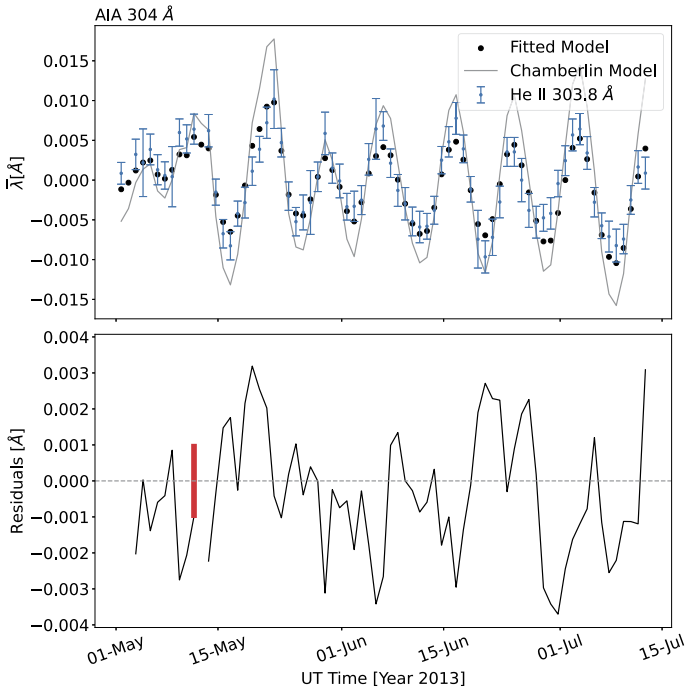


**Figure 6** The results of the inspection-of-residuals fitting for the He 303.8 Å emission line as described in the text. *Top panel* presents the measured EVE centroids (*blue*), the model output (*black*), and the Chamberlin model (*grey*, see Equation 9). Specifically, in these figures, the Chamberlin model has been corrected using the fitted background term  $C_2t$ . The *bottom panel* shows the residuals (*black*) between the EVE measured centroids and the output model with the Gaussian equivalent width  $\epsilon$  (*red*). See Table 1 for the parameters used in the centroid extraction, and Table 3 for the fit parameters. The Doppler RMS of the background-corrected EVE centroids (see Figure 8) is approximately  $4\text{--}5\text{ km s}^{-1}$  for this line over the time considered.

Figure 9 presents the results of inspection-of-residuals fitting of the astigmatism for He II 303.7860 Å over the four years of MEGS-A operations. The results are compared with the results of the cruciform scans over the same time period. For our fits, we divide the data into 55-day intervals, with the centroids sampled daily between the hours of 17:00–18:00 UT. As above, further centroid-extraction parameters are provided in Table 1. The grid-search is again performed using Equation 8, over the parameter ranges  $C_0, C_1 \in [0, 40]$ , and  $C_2 \in [-10, 10]$ , with 25 equidistant samples in each range. The procedure is iterated over 100 bootstrap resamples of the residual distributions. The value of  $\epsilon$  is set to the minimum of the measured errors for each interval, although for repeated fittings the structure of the output parameters is not sensitive to the exact choice of this value. In the figure, the grey-shaded region indicates the time of the bakeout of the EVE CCD, which is responsible for the discontinuity in the derived cruciform-scan coefficients.

The results show reasonable agreement for the quadratic coefficient over the four-year time interval using our independent technique. However, we observe that the fitted quadratic coefficients are often lower than that expected from the cruciform data; with increasing disagreement towards the end of the MEGS-A lifetime. Chamberlin (2016) notes that any non-uniformities on the Sun (such as ARs) should not affect the results of the cruciform scans, since the wavelength offsets computed are relative measurements, and so this is not

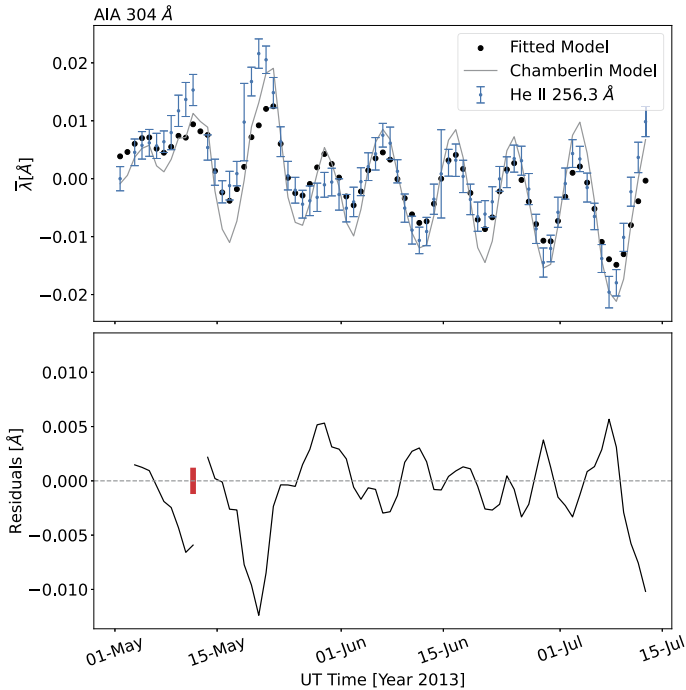


**Figure 7** Similar to Figure 6, the output model of the fitting to the measured centroids of He II at 256.3 Å. The *top panel* presents the measured EVE centroids (*blue*), the model output (*black*), and the Chamberlin model (*grey*, see Equation 9). The *bottom panel* shows the residuals (*black*) between the EVE measured centroids and the output model, with the Gaussian equivalent width  $\varepsilon$  (*red*). As above, see Table 1 for the parameters used to measure the line centroid, and Table 3 for the fit parameters. The Doppler RMS of the background-corrected EVE centroids (see Figure 8) is in the vicinity of 9–10 km s<sup>-1</sup> for this line over the time considered.

likely to be the source of discrepancy in this case. The first highlighted data point (coloured purple, enumerated 1) suggests that the measured EVE wavelength shifts are ill-described by the image-centroid basis functions and so the significant deviation from the cruciform values is expected. It may be that other components not considered in the model are distorting the wavelength shifts. For example, the He line considered may also be affected by the blending of the nearby hotter Si II line at 303.3250 Å. Indeed, for the later models, (enumerated 2, 3) despite the reduction in the fitted quadratic coefficients with respect to the cruciform values, the Chamberlin model does not significantly differ from the best-fit model.

For the linear coefficient in  $Y$ , the deviation from the cruciform scan values is somewhat expected. As noted, this coefficient corresponds to north–south on the solar surface (the cross-dispersion direction of the MEGS-A grating), while the  $X$ -coefficient corresponds to east–west (the dispersion direction). To provide a good fit to the data, it is necessary that there be sufficient variation in the image-centroid basis functions  $\bar{Y}^1(t)$ . AR activity is primarily concentrated around the solar Equator, with much less variation north–south over the time periods considered in the fittings, with respect to the obvious large east–west variations due to the rotation of the Sun. Our investigations have found that the structure of the models are only weakly dependent on the linear term in  $Y$ . A combination of these facts may contribute to the significant deviations from the cruciform values in Figure 9.

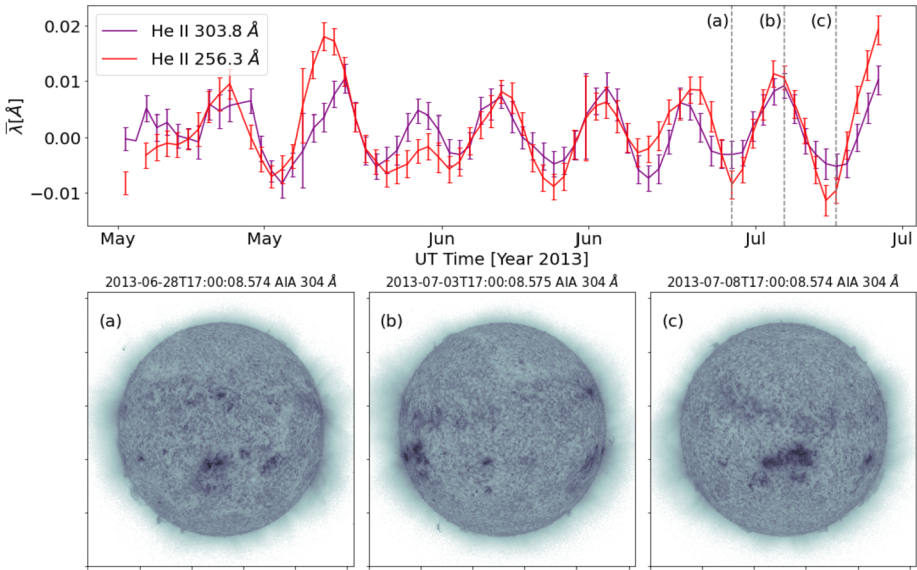


**Figure 8** A comparison of the (background corrected) time series of the two He II lines considered in Figures 6 and 7. The *top panel* displays the wavelength shifts of He II 303.8 Å (*purple*) and He II 256.3 Å (*red*), with the equivalent Doppler RMS being approximately 4–5 km s<sup>-1</sup> and 9–10 km s<sup>-1</sup> for each signal respectively. Note the similar wavelength amplitudes of the astigmatism-induced oscillations. The *bottom panel* shows corresponding AIA images at the times of extrema (*labelled grey dashed lines in the top panel*). The minima correspond to AR activity near disk centre, while the maxima correspond to AR activity at the limbs.

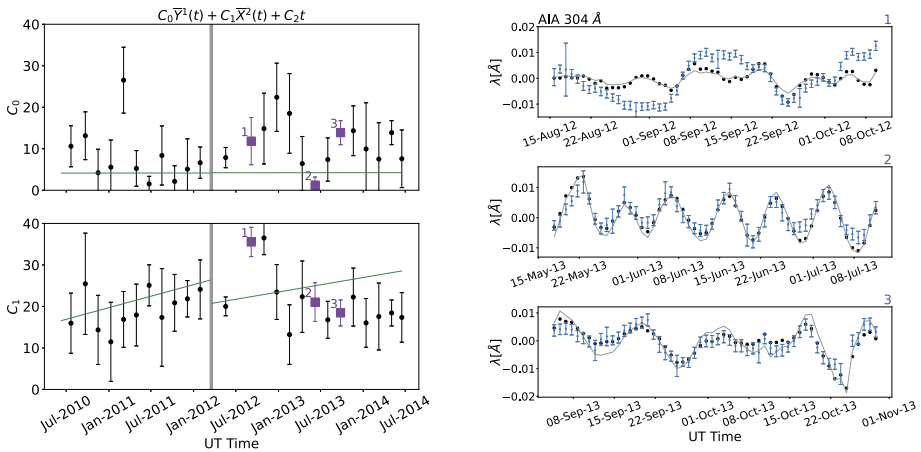


**Figure 9** *Left*: the fitted astigmatism coefficients  $C_0$  (*top panel*) and  $C_1$  (*bottom panel*) from the inspection-of-residuals fitting to He II 303.8 Å wavelength shifts over the four years of MEGS-A operations. The data points are plotted at the centres of the intervals. The approximate time of the CCD bakeout is indicated by the *grey shaded region*. Also shown are the coefficients derived from the cruciform scans (*green solid lines*). For clarity, the fitted background coefficients  $C_2$  are omitted. *Right*: corresponding intervals corresponding to the enumerated *purple (square)* data points in the *left panels*; in each panel, He II 303.8 Å wavelength shifts are displayed in *blue*, the fitted model in *black*, and the Chamberlin model in *grey*.

We have established that a component of the oscillatory structures in MEGS-A observed wavelength shifts can be attributed to the instrumental astigmatism. In the following sections, we investigate the apparent flows in solar active regions. Our treatment of the astigmatism now allows us to extend previous analyses in the literature to lines observed with MEGS-A.

### 3. Analysis of Hot Flows with Both MEGS-A and MEGS-B

#### 3.1. Modelling the Flow: How Fast Can It Be?

We now present a simple Doppler model that is sufficient to characterise the wavelength shifts of a range of lines observed by both MEGS-A and MEGS-B over a broad range of wavelengths and temperatures. As demonstrated, our treatment of the instrumental astigmatism allows us to extend the analysis to lines in MEGS-A, where both astigmatism and flow-like components can contribute to the shifts. In this and all subsequent sections, we restrict our attention to the epoch spanning 1 August 2012 to 25 September 2012. All AIA images are sampled at 17:24 UT daily, and line-centroids evaluated between 17:00 and 18:00 UT. We note that this time interval is representative, and the following analysis should apply over the entire database of MEGS operations.

We define the model accounting for astigmatism, flow-like components, and the secular background term:

$$\Delta v_{\text{AIA}} [\text{pm}] = C_0 \bar{A}(t) + C_1 \bar{F}(t) + C_2 t, \quad (10)$$

where  $\bar{A}(t)$  is as defined in Equation 9, with new roles for  $C_0$  and  $C_1$  as shown, with the background term unchanged and assigned to  $C_2$ . This form of correction assumes astigmatism contributions of a comparable size to those derived by Chamberlin (2016), and we allow for a wavelength dependence by searching for good fits with perturbations of  $C_0$  away from unity. Recall that Equation 6 defines the flow image-centroid as

$$\bar{F} = \sum_{i,j} \frac{I_{ij} F(X_{ij})}{I_{\text{tot}}}. \quad (11)$$

We consider the simple flow model according to

$$F(X_{ij}) = (-1 + 2H)X_{ij}^2, \quad (12)$$

for pixel coordinates  $i, j$ , where  $H$  is a step function such that  $H = 1$  or  $0$  for  $[X_{i,j} > 0]$  or  $[X_{i,j} < 0]$ , respectively, with the sign convention as defined in Section 2.1. This simplest-possible model for the flow term assumes uniform horizontal flow over the time interval considered, with different line-of-sight directions in the eastern and western hemispheres. It is likely true that different active regions on the solar surface could exhibit different flow speeds; indeed, the flows may not even be constant over the evolution of a single active region. In any case, this simplified treatment characterises the wavelength shifts surprisingly well (see Figures 10, 11, 12, 14). Depending on which instrument observes the line, we consider restrictions on the model as follows: MEGS-B exhibits no astigmatism, and so  $\bar{A}(t)$  is neglected. Further, the wavelength shifts of lines in MEGS-A demonstrate no background shifts over this period, and so the secular term is removed in this case.



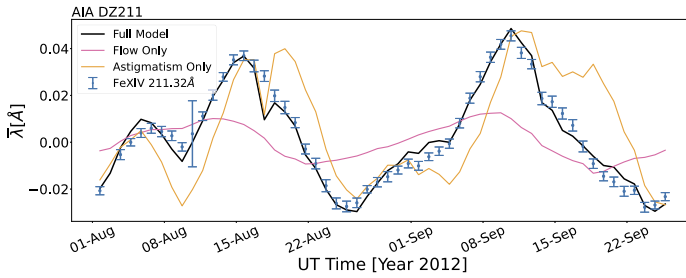


**Figure 10** The results of the inspection-of-residuals fitting to the Fe XIV line at 211.3170 Å. We perform the grid-search over the parameter ranges  $C_0 \in [0, 2]$ ,  $C_1 \in [0, 25]$ , with 25 equidistant samples in these ranges and iterate over 100 bootstrap resamples of the residual distributions. Plotted are the measured wavelength shifts observed by EVE, the results of the full model fitting, the flow-only fitting, and the astigmatism-only fitting (as indicated in the figure legend). We find good agreement with the inclusion of both astigmatism and flow-like components in the model. The image-centroid basis functions are derived from the DZ211 images as described in the text. The Doppler RMS of the Fe XIV line-motion for this time interval is around  $24\text{--}25\text{ km s}^{-1}$ .

We first demonstrate that the inclusion of both the simplified flow term and the astigmatism is necessary to describe the observed Doppler shifts in MEGS-A. Figure 10 presents the results of a fitting of the relevant coefficients in Equation 10, to the wavelength shifts of Fe XIV at 211.3170 Å over the 2012 epoch using the inspection-of-residuals procedure. Some details of the fitting are given in the figure caption, and the results are consistent with the fittings described in Section 3.2. This line falls in the MEGS-A spectral range, and so it experiences some astigmatism. We neglect the background term during the fitting as described above. As a proxy for the EUV intensity distributions of this line on the solar disk, we consider the approximation derived by Del Zanna (2013) that estimates the contributions to the 211 Å AIA passband due to the Fe XIV line. This takes the form of a linear combination of AIA passbands:

$$I(\text{Fe XIV}) = I(211 \text{ \AA}) - I(171 \text{ \AA})/17 - I(193 \text{ \AA})/5, \tag{13}$$

and such images are hereafter labelled “DZ211”. The image-centroid basis functions as defined in Equation 10, are computed using the DZ211 images for this fitting. Also presented in the figure are the best fits in the flow-only case (setting  $C_0 = 0$ ) and the astigmatism-only case (setting  $C_1 = 0$ ). Our findings suggest that both the flow-like and astigmatism contributions are necessary to characterise the wavelength shifts of this line; with good agreement only possible with the inclusion of both terms in the fitting. In fact, an identical treatment provides good fits for the Doppler shifts of many other Fe lines observed with MEGS-A (see Figure 12). The output parameters of this fitting are listed in Table 4. A non-zero flow term for this line is expected, with observations from Hudson et al. (2022) indicating that the flows become detectable mainly at higher temperatures.

In a similar fashion, we can supplement imaging from other appropriate AIA channels in the computation of the image sums. In some cases, this can provide better shape-wise fits to observed Doppler profiles. By design, the 94 Å AIA passband observes Fe XVIII in flaring plasma (Lemen et al., 2012), and this ion is also the dominant contributor in AR plasma (O’Dwyer et al., 2010). We nevertheless find that image centroids derived from the 94 Å channel also work well to describe the wavelength shifts of many of the lines observed by EVE. Figure 11 demonstrates this fact in the fitting of the pair of Mg X ions at 609.7930 Å and 624.9410 Å. These lines fall in MEGS-B and so we neglect the astigmatism

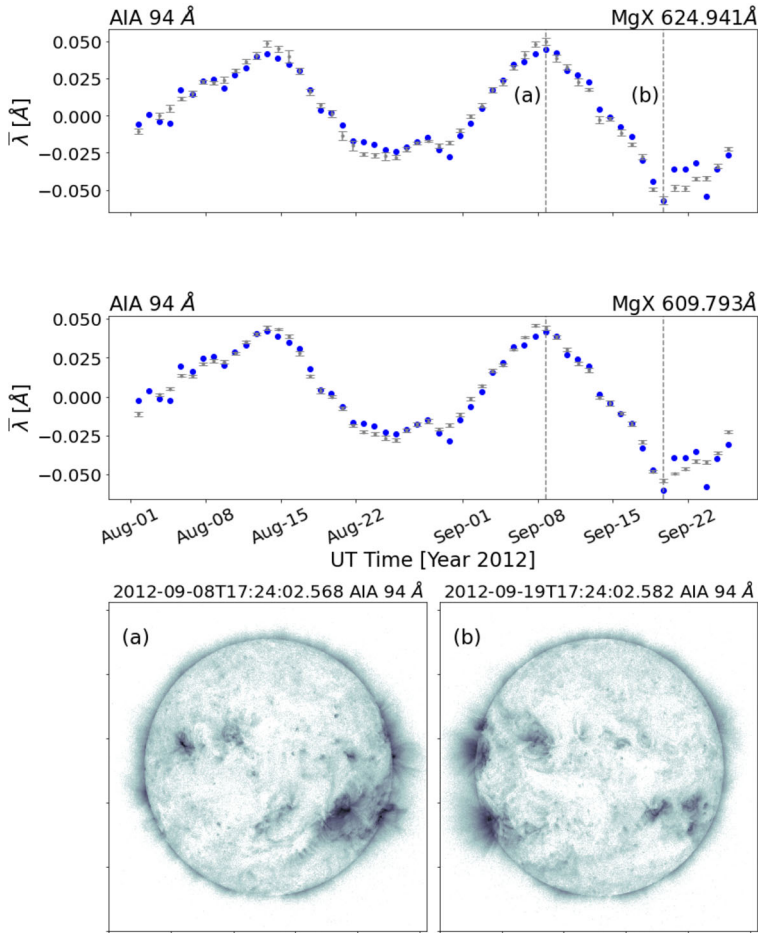


**Figure 11** The results of the inspection-of-residuals fitting to the Mg x line pair at 609.7930 Å (*second panel*) and 624.9410 Å (*top panel*), respectively. The grid search is performed over the parameter ranges  $C_1 \in [0, 50]$ ,  $C_2 \in [-20, 0]$  with 25 equidistant samples in each range and the procedure iterated over 100 bootstraps. The plot shows the measured wavelength shifts observed by EVE (*grey error bars*) and the results of the full model fitting (*blue*). The Doppler RMS of the Mg x line-motions are in the vicinity of  $14 \text{ km s}^{-1}$  for both ions over the time considered. Image-centroid basis functions are derived from 94 Å AIA images. The corresponding AIA images at the time of a local maxima and minima (labelled) are presented in the *bottom panels*. Notably, maxima correspond to AR at the west limb, minima at the east, indicative of the presence of prograde flows.

term. We find that the simplified flow-model using the 94 Å AIA imaging well describes the large Doppler swings of each of the Mg x ion pair. The prograde nature of the apparent flows also clearly appears in the figure, with the maxima and minima corresponding to AR activity peaking at west/east limbs respectively. Notably, we see similar shape-wise behaviour between the two ions, and in the magnitude of the derived flow coefficients. In this analysis, we use AIA images as proxies for actual monochromatic images. The choice of which band to use for this purpose may not strongly affect the results, because active regions appear prominent against the QS background in all bands considered. The fits cannot be used

for quantitative Doppler measures, however, because the AR contrast against the (assumed stationary) large-scale corona will depend upon the AIA band chosen. We will explore the role of image choice further in the model-fittings in the following section.

### 3.2. Multi-wavelength Fits: Dependence on Formation Temperature

Our findings demonstrate that the simplified model defined in Section 3, Equation 10 is well able to characterise the wavelength shifts of lines observed with both MEGS-A and MEGS-B. We seek to extract the dependences of the flow component on the plasma temperature and wavelength, and so we select a range of lines observed with EVE over a broad range of these parameters. Table 1 lists the centroid-extraction parameters for all lines considered, while Table 4 lists the results of the fitting for each, which we discuss below. By performing an inspection-of-residuals procedure completely analogously to treatments described above, we fit the relevant coefficients in three different cases; supplementing the different image-types: DZ211, AIA 94 Å, and AIA 304 Å into the computation of the image-centroid basis functions.

For all of the lines considered, we perform grid searches over the ranges listed in Table 5. The differing ranges are linked with the varying amplitudes of the centroids of differing image-types. This will be discussed more fully later in the text. Identically in all fittings, we consider 25 equidistant samples in each of the ranges, and iterate the procedure for 100 bootstrap iterations of the residual distributions. The values of  $\varepsilon$  are also listed, in each case; this is taken as the median of the uncertainty distribution of the weighted-centroids of the particular line over the 2012 epoch.

Figure 12 presents the model fittings to the observed wavelengths of Fe ions in MEGS-A. The parameters for each model are listed in Table 5. This demonstrates systematically that our simplified model can sufficiently characterise the Doppler shifts of many different Fe lines. The DZ211 images provide the best global fits in nearly all cases, and our findings conclude that reasonable agreement is also possible using the 94 Å and 304 Å passbands. We do not show other fits for Fe IX 171.07 Å using imaging from the AIA 171 Å passband. These show slight improvements, as expected, since this ion is the dominant contributor for QS and AR plasmas (O'Dwyer et al., 2010). Although it is not possible from these data to extract an absolute wavelength dependence of the astigmatism, Figure 13 suggests a significant increase in the derived astigmatism coefficient for increasing wavelength. We observe this structure in the fittings derived from all image-types considered.

Figure 13 points to a monotonically increasing wavelength dependence away from the Chamberlin (2016) result for 304 Å. Unfortunately the scaling depends upon the chosen image reference in our technique. Without access to monochromatic images, we cannot interpret this result directly as a property solely of the astigmatic correction, rather than a property of the image concentration (decrease of AR contrast with wavelength). Accordingly we do not quote a general result here, but only note that the correction appears to increase significantly as a function of wavelength.

Similarly, Figure 14 presents the output of the models for all the lines falling into MEGS-B. For this instrument, the effects of the astigmatism are neglected in the model. As before, we find good agreement between the models and observed line-motions for many of the ions in the analysis. The best global fits are found for lines with larger-amplitude Doppler swings, using the 94 Å and 304 Å passbands. The Doppler shifts are characteristic of prograde flows, with similar line behaviour for the same-ion line pairs: Fe XVI 335.4090 and 360.7500 Å, Mg X 609.7930 and 624.9410 Å, and Si XII 499.4060 and 520.6650 Å.

For all lines considered, we find differing magnitudes of the modelled coefficients  $C_0$  and  $C_1$  for the best-fits to the data when supplementing different AIA passbands. Naturally,

**Table 4** The output parameters of the multi-wavelength flow fittings. The *first to third columns* are identical to Table 1; the coefficients  $C_j$  are as defined in Equation 10, and the AIA images used to construct the models are listed below each parameter in the header; the value of  $\epsilon$  is listed for each line, and is computed via the median of the measured uncertainty distribution of each line over the 2012 epoch. The \* denotes the flow-only fitting as described in the text, while the \*\* denotes the astigmatism-only fitting. Above the *divide* corresponds to lines in MEGS-A; below, lines in to MEGS-B.

Ion	$\lambda$ -CHIANTI [Å]	$\log(T_{\max})$	$C_0$	$C_0$	$C_0$	$C_1$ [pm]	$C_1$ [pm]	$C_1$ [pm]	$C_1$ [pm]	$\epsilon$ [Å]
			DZ211	94	304	DZ211	94	304	304	
Fe IX	171.0730	5.9	0.17 ± 0.12	0.75 ± 0.35	1.46 ± 0.87	2.08 ± 1.04	4.16 ± 2.08	7.50 ± 5.33	0.002	
Fe XI	182.1670	6.2	0.25 ± 0.16	0.63 ± 0.47	1.04 ± 0.80	1.56 ± 1.04	5.20 ± 5.76	10.00 ± 11.53	0.003	
Fe XII	195.1190	6.2	0.37 ± 0.26	0.78 ± 0.79	3.13 ± 1.09	4.16 ± 2.33	8.33 ± 3.89	25.00 ± 6.20	0.001	
Fe XIII	209.6190	6.3	0.41 ± 0.24	1.13 ± 0.52	1.88 ± 0.98	4.16 ± 1.74	10.42 ± 2.63	25.00 ± 6.69	0.003	
Fe XIV	211.3170	6.3	1.00 ± 0.14	1.75 ± 0.48	2.522 ± 1.57	7.29 ± 1.06	17.18 ± 3.84	50.00 ± 15.31	0.002	
Fe XIV*	211.3170	6.3	n/a	n/a	n/a	3.65 ± 7.09	n/a	n/a	0.002	
Fe XIV**	211.3170	6.3	1.50 ± 0.60	n/a	n/a	n/a	n/a	n/a	0.002	
Fe XIV	274.2030	6.3	1.00 ± 0.26	1.25 ± 0.35	2.91 ± 0.94	5.21 ± 2.65	12.50 ± 2.97	30.00 ± 13.79	0.004	
Fe XV	284.1630	6.8	1.33 ± 0.18	1.88 ± 0.51	4.58 ± 1.43	3.13 ± 1.36	15.10 ± 4.46	50.00 ± 25.89	0.002	
			$C_1$ [pm]	$C_1$ [pm]	$C_1$ [pm]	$C_2$ [pm yr <sup>-1</sup> ]	$C_2$ [pm yr <sup>-1</sup> ]	$C_2$ [pm yr <sup>-1</sup> ]		
			DZ211	94	304	DZ211	94	304		
Fe XVI	335.4090	6.8	6.25 ± 2.88	14.58 ± 5.07	60.00 ± 7.86	-10.00 ± 5.54	-10.00 ± 3.80	-10.00 ± 0.83	0.010	
Fe XVI	360.7500	6.8	9.375 ± 3.27	17.70 ± 5.23	55.00 ± 17.32	-1.04 ± 4.23	-4.16 ± 5.01	-5.83 ± 4.42	0.005	
Mg IX	368.0710	6.0	3.125 ± 1.71	6.25 ± 2.37	15.00 ± 10.07	-6.04 ± 5.43	-5.00 ± 3.45	-10.00 ± 5.79	0.004	
Si XII	499.4060	6.9	16.67 ± 2.39	28.13 ± 6.27	95.50 ± 17.29	-10.00 ± 6.21	-12.91 ± 4.40	-17.50 ± 6.74	0.001	
Si XII	520.6650	6.9	19.27 ± 3.08	37.50 ± 6.57	107.50 ± 13.02	-7.91 ± 4.23	-10.21 ± 6.07	-5.41 ± 4.12	0.001	
Mg X	609.7930	6.8	13.54 ± 2.85	25.00 ± 2.74	70.00 ± 7.61	-5.83 ± 5.58	-16.25 ± 4.67	-14.16 ± 5.09	0.001	
Mg X	624.9410	6.8	14.06 ± 2.95	25.52 ± 6.52	80.00 ± 13.79	-5.63 ± 5.13	-11.46 ± 6.39	-8.95 ± 6.37	0.002	
Ne VIII	780.3850	5.8	1.56 ± 1.06	3.125 ± 2.62	10.00 ± 7.39	-5.00 ± 5.33	-4.17 ± 5.03	-4.58 ± 5.25	0.006	

**Table 5** The ranges of parameters over which the inspection-of-residuals grid-search is performed for the modelling in Section 3. As explained in the text, lines in MEGS-A neglect the secular coefficient  $C_2$  in the search, while lines in MEGS-B neglect the astigmatism coefficient  $C_0$ .

Image-type	$C_0$	$C_1$ [pm]	$C_2$ [pm yr <sup>-1</sup> ]
DZ211	[0, 2]	[0, 25]	[-20, 0]
AIA 94 Å	[0, 3]	[0, 50]	[-20, 0]
AIA 304 Å	[0, 5]	[0, 120]	[-20, 0]

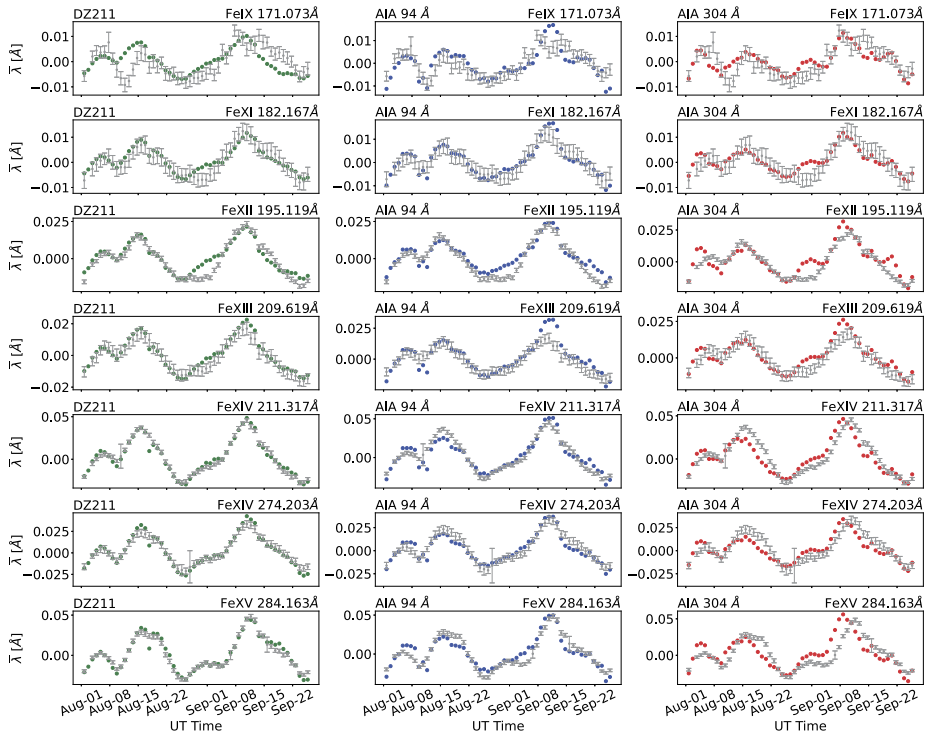
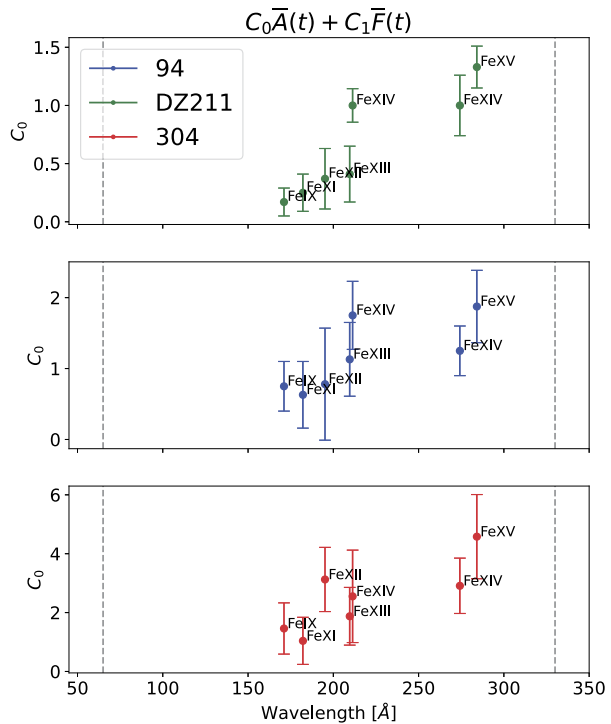


**Figure 12** The corresponding output models of the inspection-of-residuals parameter fittings to the line-motions of Fe ions residing in MEGS-A. Fitted coefficients for each ion are listed in Table 4. *Columns left to right* display the output models from fittings using the image-types DZ211 (green scattered), AIA 94 Å (blue scattered), and AIA 304 Å (red scattered), respectively. Grey errorbars denote the centre-of-mass line centroids extracted for each ion over the 2012 epoch; *descending rows* correspond to fittings of different ions labelled in the panel titles.

different images will generate different image-centroid basis functions. While those considered in this article all exhibit dominance of active-region (AR) presence over quiet Sun (QS) to some degree, variations in the AR/QS ratio are present between the image types. As an example, the Doppler swings of  $\bar{F}(t)$  are larger for those computed for the DZ211 images than for those derived from the raw 304 Å passband. In consequence, an increase in the size of  $C_1$  is required to fit the observed Doppler profiles for modelling with the latter. In contrast, the  $C_1 \bar{F}(t)$  component of the output models is similar in magnitude between image-types. This is expected behaviour, since they are modelling the same Doppler shifts

**Figure 13** The derived astigmatism coefficient  $C_0$  mapped against wavelength for each Fe line residing in MEGS-A. *Descending rows* display the corresponding output coefficients using the indicated image types. *Dashed lines* highlight the wavelength bounds of the MEGS-A instrument. A clear increase in  $C_0$  is visible for increasing wavelength for the ions considered. Errorbars are derived from the bootstrapping procedure as described in the text.



for a given line. The same observations are analogously true for the astigmatism term, and derived coefficients thereon. This explains, for example, the necessary increase in parameter ranges in the grid-search visible in Table 5; the increasing magnitude of the derived coefficients  $C_0$  and  $C_1$  in Table 4 from DZ211, 94 Å to 304 Å; and the differences in derived astigmatism coefficient  $C_0$  between image-types in Figure 13. To emphasise, the increase in grid-search ranges does not cause the increase in fitted parameters, but rather the ranges are tightened for modelling with the DZ211 and 94 Å images with respect to the 304 Å images in order to increase the resolution in the grid-search.

To explore the dependence of the derived flow coefficient  $C_1$  on wavelength and line-formation temperature, we compute the maximum redshifts of the modelled flow-components for each line over the 2012 epoch. This value is evaluated according to  $\max(C_1 \bar{F}(t))$ , where  $C_1$  here denotes the *output* coefficient  $C_1$  of the inspection-of-residuals fitting procedures. Figure 15 presents this quantity as mapped against temperature and wavelength separately. Pearson correlation coefficients reveal the strong correlation between flow-speed and temperature of the line formation. Specifically, we find a monotonic increase in flow speed against the listed CHIANTI  $T_{\max}$  for each line, with maximum flow speeds for this epoch computed at around  $40 \text{ km s}^{-1}$ . These data do not allow us to determine the actual speed of the plasma flow, so this represents a lower limit. We do not detect a dependence on wavelength, which could have suggested a systematic bias.

## 4. Conclusions

This article extends the analysis of EVE Doppler signatures on active-region time scales of days to weeks, as reported earlier for the MEGS-B data by Hudson et al. (2022). The initial

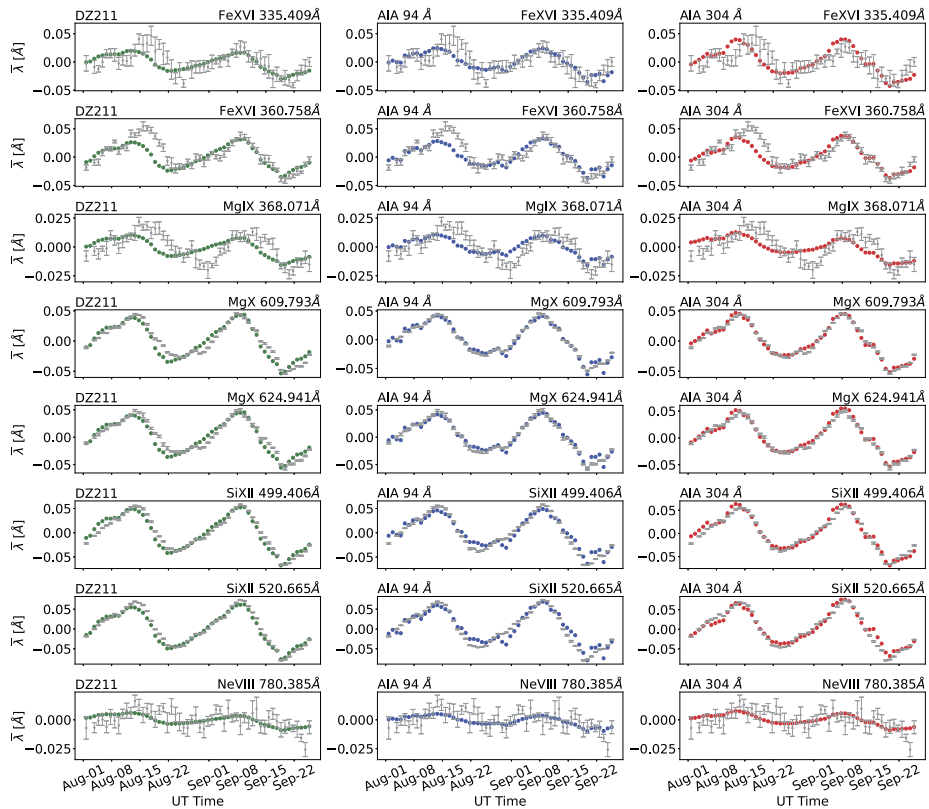


**Figure 14** An analogous presentation of the output models as in Figure 12. Presented here are the final output models of the ions falling into MEGS-B, where the astigmatism effects are neglected.

results described an unexpected finding: the EVE Sun-as-a-star data show large Doppler variations for hot active-region lines. At EVE’s spectral resolution, the hot lines are bodily shifted relative to the cold lines formed in the transition region or at lower temperatures. The hot lines show strong redshifts when images show E-limb emission, such as when a new isolated active region rotates onto the disk, and corresponding blueshifts at the W limb. The simple and satisfactory explanation for this consists of prograde (from E to W) flows within individual active regions.

Because MEGS-B could only detect six appropriately hot lines, the present article focuses on MEGS-A with its numerous hot lines from many species. In these data, astigmatism in the optics competes with the true Doppler signatures. We have studied one particular epoch in full detail, fitting multiple parameters to disentangle the systematic effects from the signatures of the flows detected by Hudson et al. (2022). The results confirm the conclusion that Sun-as-a-star EUV spectroscopy shows high-speed prograde Doppler flows in active-region structures, and furthermore establish a pattern of Doppler velocity increasing with line-formation temperature. The flow speeds reported here represent lower limits for three specific reasons: confusion from competing flows, dilution by any diffuse quiet-Sun emission, and projection onto the line of sight. All of these effects conspire to reduce the observed flow speed. We therefore cannot provide quantitative results on the actual flow speeds and must wait for imaging spectroscopy to provide this key information.

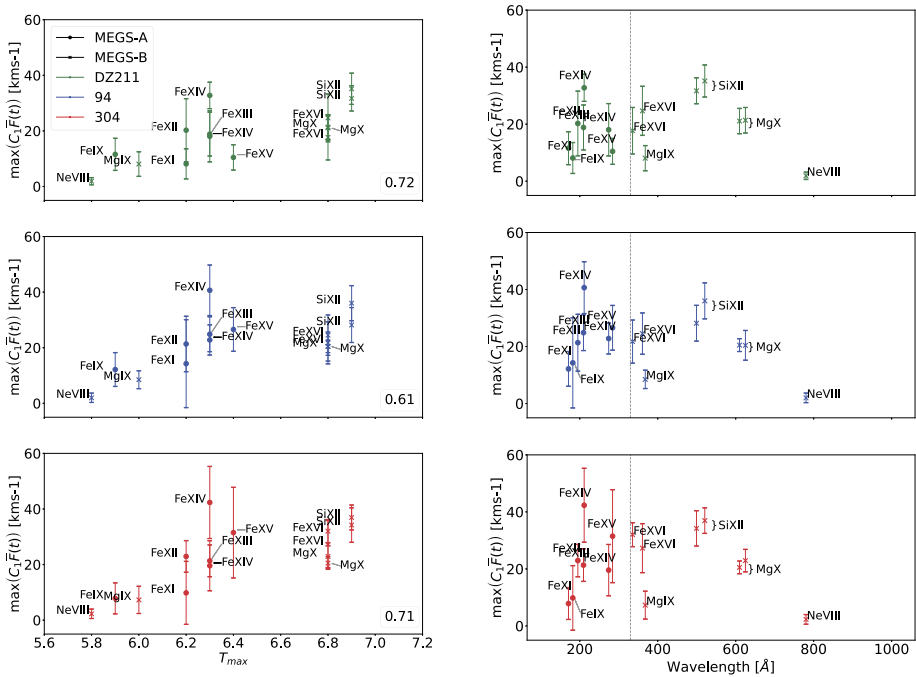


**Figure 15** Parameter dependences of the maximum redshifts of modelled flow components with (left) the listed CHIANTI  $T_{\max}$  of the line (Pearson correlation coefficients indicated in each panel); and (right) the CHIANTI wavelength. We see a strong positive correlation between temperature and flow-speed, but none with wavelength. The grey dashed lines in the left panels indicate the boundary between MEGS-A and MEGS-B. Error bars are derived from the bootstrapping procedure and propagated through the Doppler conversions.

To summarize:

- We have confirmed the analysis of MEGS-A astigmatism by Chamberlin (2016), based on the cruciform-scan maneuvers of the SDO spacecraft. Our analysis independently uses AIA image distributions, rather than the off-pointing data from the cruciform scans. We extend Chamberlin’s formulae to helioprojective coordinates (Equation 9) and derive related fits for lines other than He II 304 Å.
- With parametrized models for the MEGS-A astigmatism, we fit a simple model for steady AR flows and again detect their prograde character, thus independently confirming the MEGS-B result previously published.
- We find a monotonic increase of flow speed with line-formation temperature. This hints at a relationship with the sound speed.

We do not have an explanation for the hot prograde flows, but again note that they favor the direction of field-aligned siphon flow in the leader/follower asymmetry of active regions. We speculate that these flows have significant relationships with the physics of coronal heating and the generation of plasma turbulence. The simple model that we have used captures the essential property of the prograde flow, but as Figure 12 illustrates in detail, small systematic deviations do exist. These may help future studies to learn more from the Sun-as-a-star viewpoint via image comparisons (including DEM analysis) of the active regions, especially during the four years (2010–2014) of MEGS-A data availability. More



may also be learned directly from the EVE data themselves, for example in detailed work with line profiles; these data have high photon throughput, resulting in high precision, and the analyses to date have not taken full advantage of this.

**Acknowledgments** We acknowledge the use of JPL Horizons ephemeris data, and the CHIANTI spectroscopy database (Dere et al., 1997). We thank Phil Chamberlin, Tom Woods, and the EVE team for advice and commentary. The School of Physics and Astronomy, University of Glasgow supported J. Fitzpatrick for this student project in Summer 2022. H. Hudson thanks Lyndsay Fletcher for discussion and advice. This article and our earlier one benefited from student work in the School's Honours Astronomy laboratory course, under the general direction of Graham Woan.

**Author contributions** J.C. Fitzpatrick and H.S. Hudson wrote the main manuscript text and J.C. Fitzpatrick prepared the figures. Both authors have reviewed the manuscript. Data courtesy of NASA/SDO and the AIA and EVE science teams.

**Data Availability** All of the data used in this article are in the public domain.

## Declarations

**Competing interests** The authors declare no competing interests.

**Open Access** This article is licensed under a Creative Commons Attribution 4.0 International License, which permits use, sharing, adaptation, distribution and reproduction in any medium or format, as long as you give appropriate credit to the original author(s) and the source, provide a link to the Creative Commons licence, and indicate if changes were made. The images or other third party material in this article are included in the article's Creative Commons licence, unless indicated otherwise in a credit line to the material. If material is not included in the article's Creative Commons licence and your intended use is not permitted by statutory regulation or exceeds the permitted use, you will need to obtain permission directly from the copyright holder. To view a copy of this licence, visit <http://creativecommons.org/licenses/by/4.0/>.

## References

- Andrae, R.: 2010, Error estimation in astronomy: a guide. [arXiv](#). [ADS](#).
- Andrae, R., Schulze-Hartung, T., Melchior, P.: 2010, Dos and don'ts of reduced chi-squared. [arXiv](#). [ADS](#).
- Brown, S.A., Fletcher, L., Labrosse, N.: 2016, Doppler speeds of the hydrogen Lyman lines in solar flares from EVE. *Astron. Astrophys.* **596**, A51. [DOI](#). [ADS](#).
- Chamberlin, P.C.: 2016, Measuring solar Doppler velocities in the He II 30.38 nm emission using the EUV Variability Experiment (EVE). *Solar Phys.* **291**, 1665. [DOI](#). [ADS](#).
- Cheng, Z., Wang, Y., Liu, R.: 2021, Correcting Doppler shifts in He II 30.38 nm line by using the EVE and AIA data from Solar Dynamics Observatory. *Astrophys. J.* **911**, 36. [DOI](#).
- Cheng, Z., Wang, Y., Liu, R., Zhou, Z., Liu, K.: 2019, Plasma motion inside flaring regions revealed by Doppler shift information from SDO/EVE observations. *Astrophys. J.* **875**, 93. [DOI](#). [ADS](#).
- Crotser, D.A., Woods, T.N., Eparvier, F.G., Triplett, M.A., Woodraska, D.L.: 2007, SDO-EVE EUV spectrograph optical design and performance. In: Fineschi, S., Viereck, R.A. (eds.) *Solar Physics and Space Weather Instrumentation II, Soc. of Photo-Opt. Instrument. Eng. (SPIE)* **CS-6689**, 66890M. [DOI](#). [ADS](#).
- Del Zanna, G.: 2013, The multi-thermal emission in solar active regions. *Astron. Astrophys.* **558**, A73. [DOI](#). [ADS](#).
- Dere, K.P., Landi, E., Mason, H.E., Monsignori Fossi, B.C., Young, P.R.: 1997, CHIANTI – an atomic database for emission lines. *Astron. Astrophys. Suppl. Ser.* **125**, 149. [DOI](#). [ADS](#).
- Hodges, J.L.: 1958, The significance probability of the Smirnov two-sample test. *Ark. Mat.* **3**, 469. [DOI](#). [ADS](#).
- Hudson, H.S., Woods, T.N., Chamberlin, P.C., Fletcher, L., Del Zanna, G., Didkovsky, L., Labrosse, N., Graham, D.: 2011, The EVE Doppler sensitivity and flare observations. *Solar Phys.* **273**, 69. [DOI](#). [ADS](#).
- Hudson, H.S., Mulay, S.M., Fletcher, L., Docherty, J., Fitzpatrick, J., Pike, E., Strong, M., Chamberlin, P.C., Woods, T.N.: 2022, Fast prograde coronal flows in solar active regions. *Mon. Not. Roy. Astron. Soc.* **515**, L84. [DOI](#). [ADS](#).

- Kolmogorov, A.: 1933, Sulla Determinazione Empirica di una Legge di Distribuzione. *Inst. Ital. Attuari, Giorn.* **4**, 83.
- Lemen, J.R., Title, A.M., Akin, D.J., Boerner, P.F., Chou, C., Drake, J.F., Duncan, D.W., Edwards, C.G., Friedlaender, F.M., Heyman, G.F., Hurlburt, N.E., Katz, N.L., Kushner, G.D., Levay, M., Lindgren, R.W., Mathur, D.P., McFeaters, E.L., Mitchell, S., Rehse, R.A., Schrijver, C.J., Springer, L.A., Stern, R.A., Tarbell, T.D., Wuelsel, J.-P., Wolfson, C.J., Yanari, C., Bookbinder, J.A., Cheimets, P.N., Caldwell, D., Deluca, E.E., Gates, R., Golub, L., Park, S., Podgorski, W.A., Bush, R.I., Scherrer, P.H., Gumm, M.A., Smith, P., Auker, G., Jerram, P., Pool, P., Soufli, R., Windt, D.L., Beardsley, S., Clapp, M., Lang, J., Waltham, N.: 2012, The Atmospheric Imaging Assembly (AIA) on the Solar Dynamics Observatory (SDO). *Solar Phys.* **275**, 17. [DOI](#). [ADS](#).
- Mohd Razali, N., Yap, B.: 2011, Power comparisons of Shapiro–Wilk, Kolmogorov–Smirnov, Lilliefors and Anderson–Darling tests. *J. Stat. Model. Analytics* **2**.
- O’Dwyer, B., Del Zanna, G., Mason, H.E., Weber, M.A., Tripathi, D.: 2010, SDO/AIA response to coronal hole, quiet Sun, active region, and flare plasma. *Astron. Astrophys.* **521**, A21. [DOI](#). [ADS](#).
- Pesnell, W.D., Thompson, B.J., Chamberlin, P.C.: 2012, The Solar Dynamics Observatory (SDO). *Solar Phys.* **275**, 3. [DOI](#). [ADS](#).
- Smirnov, N.: 1948, Table for estimating the goodness of fit of empirical distributions. *Ann. Math. Stat.* **19**, 279. [DOI](#).
- Thompson, W.T.: 2006, Coordinate systems for solar image data. *Astron. Astrophys.* **449**, 791. [DOI](#). [ADS](#).
- Woods, T.N., Eparvier, F.G., Hock, R., Jones, A.R., Woodraska, D., Judge, D., Didkovsky, L., Lean, J., Mariska, J., Warren, H., McMullin, D., Chamberlin, P., Berthiaume, G., Bailey, S., Fuller-Rowell, T., Sojka, J., Tobiska, W.K., Viereck, R.: 2012, Extreme Ultraviolet Variability Experiment (EVE) on the Solar Dynamics Observatory (SDO): overview of science objectives, instrument design, data products, and model developments. *Solar Phys.* **275**, 115. [DOI](#).

**Publisher’s Note** Springer Nature remains neutral with regard to jurisdictional claims in published maps and institutional affiliations.